## GT2015-43499

# COMPARISON OF STAGGERED AND IN-LINE V-SHAPED DIMPLE ARRAYS USING S-PIV

Charles P. Brown, Lesley M. Wright, and Stephen T. McClain

Baylor University
Department of Mechanical Engineering
Waco, Texas 76798-7356
Lesley Wright@Baylor.edu

#### **ABSTRACT**

As a result of the reduced pressure loss relative to ribs, recessed dimples have the potential to increase the thermal performance of internal cooling passages. In this experimental investigation, a Stereo-Particle Image Velocimetry (S-PIV) technique is used to characterize the three-dimensional, internal flow field over V-shaped dimple arrays. These flowfield measurements are combined with surface heat transfer measurements to fully characterize the performance of the proposed Vshaped dimples. This study compares the performance of two arrays. Both a staggered array and an in-line array of V-shaped dimples are considered. The layout of these V-shaped dimples is derived from a traditional, staggered hemispherical dimple array. The individual Vshaped dimples follow the same geometry, with depths of  $\delta$  / D = 0.30. In the case of the in-line pattern, the spacing between the V-shaped dimples is 3.2D in both the streamwise and spanwise directions. For the staggered pattern, a spacing of 3.2D in the spanwise direction and 1.6D in the streamwise direction is examined. Each of these patterns was tested on one wide wall of a 3:1 rectangular channel. The Reynolds numbers examined range from 10000 to 37000. S-PIV results show that as the Reynolds numbers increase, the strength of the secondary flows induced by the in-line array increases, enhancing the heat transfer from the surface, without dramatically increasing the measured pressure drop. As a result of a minimal increase in pressure drop, the overall thermal performance of the channel increases as the Reynolds number increases (up to the maximum Reynolds number of 37000).

#### **NOMENCLATURE**

Ac	cross-sectional area of rectangular channel (= W*H)
AR	channel aspect ratio (= W / H)
$A_s$	heat transfer surface area
D	dimple diameter
$D_h$	hydraulic diameter of rectangular channel (= 4A <sub>c</sub> / P)
f	friction factor
$f_o$	friction factor of fully developed flow in a smooth
	tube
h	heat transfer coefficient
Н	channel height
HTE	heat transfer enhancement (= Nu/Nu <sub>o</sub> )
i	individual image pair

k	thermal conductivity of air
L	channel length
$N_i$	number of image pairs
$N_{\rm v}$	number of vectors within an interrogation region
Nu	channel averaged Nusselt number
$Nu_{o}$	Nusselt number of fully developed flow in a smooth tube
P	perimeter of rectangular channel $(= 2[W + H])$
$\Delta P$	pressure drop through channel (P <sub>in</sub> – P <sub>out</sub> )
$\mathbf{P}_{in}$	inlet air pressure
$P_{out}$	outlet air pressure (atmospheric pressure)
Pr	Prandtl number of air
Qin	Power supplied to heater
Qloss	Heat loss through test section walls
Re	Reynolds number coolant flow through channel (= $\rho V D_h/\mu$ )
$S_{v}$	RMS fluctuating velocity
$S_x$	streamwise spacing of V-shaped dimples
$S_{xd}$	streamwise spacing of traditional hemispherical dimples
$S_y$	spanwise spacing of V-shaped dimples
$S_{yd}$	spanwise spacing of traditional hemispherical dimples
$T_b$	bulk temperature of cooling air
$T_{\mathbf{w}}$	wall temperature
$t_{ls}$	laser separation time
$t_s$	Student's t-distribution
U	random uncertainty of velocity measurement
$\overline{u}$	time averaged velocity magnitude in x-direction
$\mathbf{u}_{\mathrm{i}}$	x-direction component of velocity for image pair, i
V	average coolant velocity
$\overline{v}$	time averaged velocity magnitude in y-direction
v'	RMS fluctuating velocity component in y-direction

y-direction component of velocity for image pair, i

time averaged velocity magnitude in z-direction

RMS fluctuating velocity component in z-direction

z-direction component of velocity for image pair, i

local velocity magnitude

width of channel

 $\begin{matrix} v_i \\ V_{xyz} \end{matrix}$ 

W

 $\overline{w}$ 

w'

w<sub>1</sub> thickness of laser light sheet

x streamwise coordinate within channel

 $\Delta x$  streamwise distance between inlet and outlet pressure

measurements

y coordinate direction normal to the channel wall

z spanwise coordinate within channel

δ dimple depth

 $\eta$  overall thermal performance

μ dynamic viscosity of air

 $\rho \qquad \text{density of air} \\$ 

ω vorticity

#### INTRODUCTION

As compressor pressure ratios and turbine inlet temperatures continue to rise in search of higher power output and overall more thermally efficient engine designs, care must be taken to ensure engine components are adequately protected. To counter the increase in turbine inlet temperature, the coolant air, siphoned from the compressor stages for use in cooling the blades, must be used efficiently and effectively. Han et al. [1] has previously performed a comprehensive study of cooling schemes applied in gas turbines. Externally, a Thermal Barrier Coating (TBC) may be applied. This TBC acts as an insulator, keeping the hot mainstream gases out of direct contact with the vanes and blades. Further, through careful placement of film cooling holes, spent coolant from within the airfoil can be ejected creating a thin layer of relatively cool air between the hot mainstream gases and the surface of the blade. This external cooling must of course be augmented with various internal cooling strategies to withstand the extreme operating conditions found in gas turbine engines.

While external cooling techniques focus on reducing the heat transfer to the airfoil, internal cooling methods use the relatively cool bleed air to increase heat transfer between the blade material and the coolant. Within areas of the blade that see the highest heat loads, for example in the leading edge stagnation region, jet impingement is used for its locally very high heat transfer enhancement. The trailing edge is typically cooled with pin fins as they both increase the surface area for heat transfer and add structural support. Conventionally, the mid-chord region is cooled with rib turbulated passages and there has been significant research performed in the optimization of these passages. More recently, however, the possibility of using dimples in place of ribs has spurred new research.

Dimples in their most basic form are simple arrays of depressions that act to increase turbulence near the surface, increasing the mixing of coolant, and in doing so, increasing the heat transfer from the surface to the coolant. The earliest, and for that matter, most research in the area of dimples has focused on simple staggered arrays of hemispherical depressions. More recently, several other dimple shapes have been investigated, including square edged cylindrical, tear drop, and Vshaped dimples. Dimples are an attractive choice for internal cooling as they provide, in general, 2 to 3 times the enhancement as a smooth channel while maintaining relatively low pressure penalties. In addition to these favorable flow characteristics, since creating a dimpled surface requires removing turbine blade material, this also results in significant weight savings for the rotating portions of the turbine stages. There are several design parameters that govern the overall cooling effectiveness of each dimpled array. The most basic parameters include: the channel's Reynolds number, the dimple depth and array density, channel height, and dimple shape.

Rib turbulators exhibit heat transfer enhancements of 2 to 5 times that of a smooth channel, but there is a significant pressure penalty, with friction factors typically in the range of 10 to 20 times that of a smooth

channel. Dimple arrays on the other hand are capable of heat transfer enhancement of 2 to 3 times that of a smooth channel, while incurring only modest pressure drops, typically producing friction factors 1 to 4 times that of a smooth channel. Therefore, dimple arrays remain an attractive cooling method to engine designers because these relatively low pressure penalties result in high thermal performances despite the moderate heat transfer enhancements.

The first study to investigate the effect a dimpled surface has on the flow was completed by Gromov et al. [2]. In this investigation, flows over a single, hemispherical dimple were considered. At low Reynolds numbers, they observed streamlines impinging on the downstream edge of the dimple and recirculating, forming two semicircular zones within the dimple cavity, with an axis of symmetry about the direction of flow. At higher Reynolds numbers, asymmetry was observed with more turbulent shedding occurring from one zone versus the other.

Lin et al. [3] performed numerical simulations of the flow inside and around an array of staggered hemispherical dimples. The simulations show two vortical structures forming within the dimple cavity, each occupying half of the dimple. This behavior is complex and dependent on the shape, depth, and arrangement of dimples as well as the flow conditions within the channel. These numerical results were confirmed experimentally by Mahmood et al. [4, 5], Ligrani et al. [6], and Won et al. [7]. Mahmood et al. [4] indicates the flow structures result in two pairs of counter rotating vortices emerging from the downstream side of each dimple, staying close to the surface, while a third counter rotating pair of vortices is ejected further into the mainstream, increasing mixing significantly.

While the counter rotating vortex pair being ejected from the diagonals of each hemispherical dimple increases mixing close to the surface, the counter rotating vortex pair being ejected from the downstream edge penetrates deep enough in to the mainstream to induce secondary flows. These larger scale secondary flows, result in more frequent mixing inside the channel, bringing cooler fluid from the core of the channel closer to the surface, increasing heat transfer. While this behavior can be seen for a single dimple, when several dimples are arranged together to form an array, this effect is further magnified, resulting in large secondary flows within the channel. The repeating pattern of dimples results in the strengthening of dimple-to-dimple effects. This allows dimples downstream to add energy into an already formed turbulent structure, increasing mixing and heat transfer as a result.

Knowledge of more conventional rib turbulated passages states that increasing the Reynolds number of the flow will increase heat transfer. While this is true, increasing the Reynolds number actually leads to a decrease in the overall heat transfer enhancement (Nusselt number ratios) for ribbed channels versus the smooth channel case [1]. In the case of an array of dimples, this is not so. Chyu et al. [8] was the first to identify the relative insensitivity of Nusselt number ratios to changes in Reynolds Number. This is of course an advantage over ribs whose Nusselt number ratios decrease with increases in Reynolds number. Moon et al. [9] confirmed this Nusselt number ratio independence with respect to Reynolds numbers. It was also noted that while the Nusselt number ratios do not vary significantly, the friction factor ratios do increase with increasing Reynolds number. This leads to a slight decrease in thermal performance with increases in Reynolds Number. While these studies were performed for Reynolds numbers less than 60,000, Kim et al. [10] further confirmed this insensitivity for Reynolds numbers up to 360,000.

Dimple depth is an important consideration when discussing dimples. Deeper dimples result in more blade material being removed, increasing weight savings, but a minimum wall thickness is required to

maintain structural integrity within a turbine blade. Burgess et al. [11], Bunker and Donnellan [12], and Won et al. [7] investigated the effect of altering the depth to print diameter ratios, covering dimple print diameter ratios within the range of 0.1 to 0.4. It was concluded that increasing the depth of the dimple increases the strength of the vortices that emerge from the dimple and increases the three dimensional turbulence in the near wall region, increasing the overall advection of heat away from the surface. This enhancement does of course come at the cost of larger pressure drops within the channel. Moon and Lau [13] performed a comprehensive study with ranges of dimple density falling between 38.5-86.5%. It was shown that as the density of the array increases, the heat transfer enhancement as compared to a smooth wall increases. The friction factor, and therefore, pressure drop, likewise increases with the density of the array. Since the friction factor increases with respect to increasing Reynolds numbers, the thermal performance suffers a slight decrease as well.

When considering the effect of channel height, it is appropriate to look at the ratio of the height of the channel to the dimple print diameter. Chyu et al. [14] was the first to perform such an analysis, with ratios ranging from 0.38 to 1.15. The heat transfer enhancement data reported shows no dependence on the height of the channel. This point was again addressed by Burgess et al. [11] who reported data for height to print diameter ratios of 0.37-1.49, where they also showed no dependence of heat transfer enhancement on channel height. Mahmood and Ligrani [5] furthered the range of data available, and showed a significant rise in heat transfer with height to print diameter ratios of 0.2, when compared to the earlier studies from Chyu et al. [14] and Burgess et al. [11]. Mahmood and Ligrani [5] reported that as the height of the channel decreased, the turbulent structures being ejected from the dimple grew in strength, leading to enhanced heat transfer on the downstream edge of the dimple.

Traditionally dimples take the shape of a hemispherical concave depression on a surface; however, there have been several studies that have tried to produce shapes that outperform this design. Perhaps even simpler than that of a hemispherical dimple is that of a cylindrical dimple. A cylindrical dimple is just that, a circular region with a flat bottom cut to a certain depth. Moon and Lau [13] performed a study to determine the heat transfer enhancement from such an array. It was shown that a cylindrical array actually has a lower friction factor than that of a hemispherical array with the same dimple depths and dimple spacing. Not only was the friction factor lower, the heat transfer enhancement was significantly higher leading to an overall higher thermal performance.

The previously mentioned trends were measured and numerically calculated with sharp edged dimples. Because of manufacturing limitations, such a sharp edged array of dimples is simply not possible. Isaev et al. [15] reported numerical data on the effect of adding a radius of curvature to the dimple edge. As the radius of curvature increases, the hydraulic losses in the channel decrease, and eventually fall below that of a smooth channel. In addition to the reduced pressure losses, the heat transfer enhancement continues to increase until a critical curvature to diameter ratio of 0.2 where it begins to slowly decrease. This leads to an optimal curvature radius of 0.2 of the diameter. Another similar design is that of a banked dimple. A banked dimple is a dimple which is surrounded by a small, raised embankment. This design was proposed by Borisov et al. [16]. Although heat transfer was enhanced by this design significantly, up to 4.5 times that as a smooth channel, it came at the cost of a friction factor that was fifty times larger than that of a smooth channel, largely due to a height to print diameter ratio of 0.16. This of course resulted in thermal performances lower than that of traditional hemispherical dimples.

The first research group to stray significantly from the typical hemispherical design was that of Chyu et al. [8]. The authors introduced a novel tear drop shape. The goal of this new shape was to reduce the separation region at the upstream edge of the dimple and to reduce the pockets of vortical structures that can remain trapped in the dimple itself. The heat transfer enhancement from the tear drop shape was slightly higher than that of the hemispherical dimples, most notably in cases where the opposite wall was dimpled as well, but not by a significant margin. Stepping further away from the traditional hemispherical designs Khalatov and Onishchenko [17] chose to experiment with square dimples as well as cylindrical dimples. It was shown that while square dimples were able to edge out hemispherical and cylindrical dimples in terms of heat transfer enhancement, it came at the cost of an increase in the friction factor. Zhou and Acharya [18] once again tested square dimples, as well as a triangle dimple oriented such that the downstream edge of the triangle was perpendicular to the flow, and the tear drop shape presented earlier by Chyu et al. [8]. The triangle design performed poorly, and again the tear drop shape was shown to perform the best in regards to heat transfer enhancement.

Another dimple design was offered by Isaev et al [15]. This design is referred to as a ditchlike cavity. Essentially this ditchlike cavity is composed of two hemispherical ends placed on a cylinder, with the side of the cylinder being recessed in to the surface. This ditchlike dimple was shown to outperform traditional dimples of the same depth and total surface area in some cases. The authors believe this is a result of tornado like vortices that emerge from the dimple, largely due to the angle at which the dimples are placed with respect to the flow.

In an effort to produce secondary flows similar to those seen in channels outfitted with V shaped ribs, a V-shaped design was proposed by Jordan and Wright [19]. This V-shaped design is similar to the ditchlike design proposed by Isaev et al. [15]. In this design, three adjacent dimples are connected, producing a V-shaped dimple. The most interesting part of this design is the fact that heat transfer enhancement increases by a significant amount as Reynolds number increases. This is the opposite of what is seen in ribbed channels as well as an improvement over traditional hemispherical dimples, which are insensitive to changes in Reynolds number. As a result of this increasing heat transfer and a low pressure penalty, the thermal performance of such a design is quite competitive with, and even exceeds angled ribs at higher Reynolds numbers.

Another interesting design is that of the deepened scale. A deepened scale is essentially a cylindrical concavity machined at an angle such that one portion of the edge is flush with the surface. This design, proposed by Liou et al. [20] was numerically shown to produce a heat transfer enhancement of 4.5 times that of a smooth surface. This is a result of a smaller vortical structure being trapped within the scale.

There has been a significant amount of research published on the topic of dimples for use in a gas turbine engine. With Nusselt number ratios in the range of 2-2.5 regardless of Reynolds number and such low friction factors associated with the heat transfer augmentation, dimples lend themselves to areas where heat loads are not high enough to justify the pressure penalty associated with ribbed turbulators.

While significant research has been performed in search of an optimal dimple design, there has been a lack of experimental work considering how these vortical structures emerging from a dimple interact with the mainstream and affect the heat transfer from the surface. This study seeks to apply the S-PIV method to further investigate the V-shaped dimple design proposed by Jordan and Wright [19]. Because the S-PIV method allows for the measurement of the 3D velocity vectors in an entire plane, a greater understanding of the interaction that each dimple has with the mainstream flow can be

gathered. Knowing how each of these features affects the flow, and how that affects the heat transfer from the surface leads to an overall better understanding of ways to further improve dimple designs, allowing engine designers to use less coolant and improve the overall efficiency of the engine. With the current investigation, average heat transfer measurements are obtained for channels with both an array of staggered V-shaped dimples and an in-line array of V-shaped dimples. To gain insight into the flow phenomena yielding this heat transfer enhancement, flowfield and turbulence measurements are obtained using S-PIV at four discrete planes within the dimple arrays. Furthermore, the effect of Reynolds number is captured (for both heat transfer and flow) over the range of 10000 to 37000 for both V-shaped dimple arrangements.

#### **EXPERIMENTAL FACILITIES**

The internal cooling test facility is comprised of a two section, single pass rectangular channel with an aspect ratio of 3:1, modified from that of Jordan and Wright [19]. The first section is simply a smooth entrance region, while the second is the heated and dimpled test section. In addition to being longer than 10 hydraulic diameters, the entrance section has two mesh screens far upstream ensuring the flow is hydrodynamically fully developed before entering the test section and the seeding particles are sufficiently dispersed to allow for accurate Particle Image Velocimetry measurements. The heated test section includes a removable wide wall that can be replaced with surfaces with various dimple geometries. With the exception of the heat transfer test surfaces, the channel has been manufactured of acrylic, providing optical access for the laser as well as the S-PIV cameras. A layout of the channel can be seen in **Figure 1**.

During heat transfer tests, all of the air that passes through an ASME square-edge orifice meter is plumbed directly in to the entrance region of the channel. While S-PIV data is being acquired, a small amount of that air is used to generate the seeding particles with a LaVision aerosol generator, and then plumbed back into the entrance region of the tunnel. The LaVision seeder is capable of producing Di-Ethyl-Hexyl-Sebacate (DEHS) oil particles with diameters on the order of 1  $\mu m$ . Particles of this size are very well suited to performing S-PIV and are known to follow even the small turbulent structures within flows. Once the air passes through the channel it is simply ejected into the lab.

To accurately determine the amount of energy that was transferred to the air by the test plates, several T-type thermocouples were used to measure the air temperature in the center of the channel immediately upstream and downstream of the heated test section. To measure friction factors, a static pressure tap was placed on the top acrylic wall near the entrance to the heated test section and a micromanometer was used to accurately measure the pressure drop.

The two dimple arrays tested in this study are also shown in Fig. 1 with details of the V-shaped geometry shown in Figure 2 [19]. The V-shaped dimple is essentially three simple hemispherical dimples combined into a single depression. The V-shaped dimple shape examined in this study is a derivation of a standard hemispherical dimple array from Griffith et al. [21]. Their traditional hemispherical array features dimple diameters of 0.635 cm (0.25 in.) and depth to diameter ratios of 0.3. In construction of the V-shaped dimples used in this study, the depth,  $\delta$ , remained the same, at 0.3D. Of course, discussing the diameter of a V-shaped dimple is not so straightforward. For the purposes of this study, the diameter of a V-shaped dimple is simply the diameter of one of the three identical hemispherical dimples used to arrive at the V shape.

Each of the dimpled heat transfer surfaces seen in Fig. 1 consists of 22 rows of V-shaped dimples. In the case of the in-line array, each

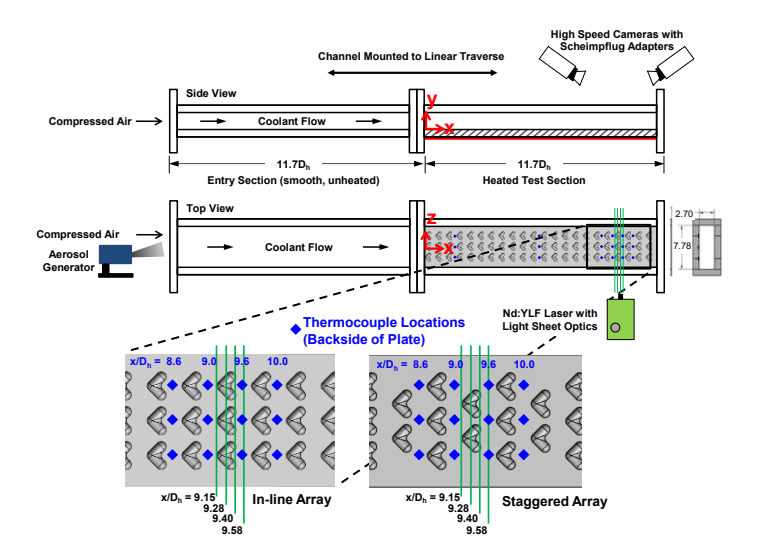


Figure 1: Overview of the Rectangular Channel

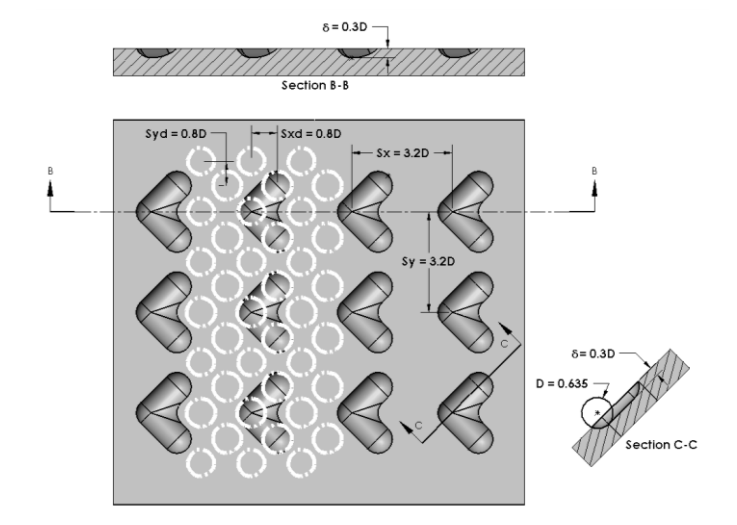


Figure 2: Details of the V-Shaped Dimple [19]

row consists of 3 V-shaped dimples. For the staggered dimple array, the first, and every other row has only 2 V-shaped dimples, while the remaining rows each consist of three V-shaped dimples. Along with the dimpled surfaces tested, a smooth surface was used to validate the results versus the Dittus-Boelter correlation. The heat transfer test surfaces are manufactured out of 1.27 cm (0.5 in.) aluminum, with the dimples milled into one of the wide surfaces using a 0.635cm (0.25 in.) ball mill. On the opposite surface, 18 holes were drilled to a depth of 1.01 cm (0.4 in.) allowing the thermocouples to be placed very near the surface of each test plate. Channels for each row of thermocouples, 0.318 cm (0.125 in.) wide and deep, were also machined into the back surface to provide an area for thermocouple wires to be routed so they would not create air gaps between the heater and the aluminum plates. Figure 2 also shows the locations of each thermocouple placed in the backside of the plates. As discussed later, only the wall thermocouples located near the channel are used. Each hole was then instrumented with a T-type thermocouple, epoxied in place with a highly thermally conductive epoxy. A 45.72 x 7.62 cm (18 x 3 in.) heater was then affixed to the back side of each aluminum surface.

During the heat transfer cases, all walls of the test section were insulated with low density styrofoam to minimize heat losses. Power to the heater was controlled using a variable transformer and varied to maintain temperatures within the bounds of the two heat loss cases. Data was recorded for Reynolds numbers of 10000, 20000, 30000, and 37000 upon reaching steady state. With three surface geometries and four Reynolds number, a total of 12 heat transfer tests were performed.

#### S-PIV Setup

The S-PIV portion of the experimental setup is more complex than that of the steady state heat transfer test performed. Figure 1 exhibits the most important aspects of the S-PIV system; the two Phantom high-speed 12 bit cameras, the LaVision aerosol generator, and the Photonics dual cavity planar laser. The cameras and laser are tied to the computer through the high speed controller to ensure the laser and cameras are operating in sync with each other. This controller is then connected to the data acquisition computer and communicates through the DaVis program.

The two Phantom V211 high-speed 12 bit cameras are capable of recording 2190 frames per second at their full resolution of 1280 x 800 pixels. However, in the current study, data was collected at only 2000 frames per second, producing a total of 1000 image pairs per camera. Each camera was equipped with a Scheimpflug adapter and a 100mm macro lens, allowing each camera to maintain a very high spatial resolution within the channel. The Scheimpflug adapter allowed the cameras to focus on a plane that was not perpendicular to the image sensor of the cameras. Because S-PIV needs an oblique angle between the cameras and the plane of interest to capture the third velocity component, these Scheimpflug adapters are required to ensure the entire plane is in focus at once.

For this study, a single LaVision aerosol generator was required to seed the channel with DEHS oil particles. To illuminate these particles, an Nd:YLF Photonics dual cavity laser was equipped with a cylindrical lens allowing it to produce a light sheet. This laser is capable of repetition rates of 10 kHz per head, however due to the limitations with the high speed cameras, data is only collected at 1 kHz per head.

The laser plane was oriented in such a way that the largest component of velocity, the streamwise velocity, was traveling perpendicularly to the laser plane. This was done to accurately capture any secondary flows that may be forming due to the repeating patterns of V-shaped dimples. Because the laser plane is very thin (  $\approx$  1 mm) and 75% of the particles must remain within the laser plane in each image pair, to produce accurate S-PIV results, the laser separation time was adjusted for each flow rate. The proper laser separation time,  $t_{\rm ls}$ , was determined with the Equation 1.

$$t_{ls} = \frac{w_l}{4V} \tag{1}$$

This resulted in a range of laser separation times of 10 to 66 microseconds depending on the flow rate of the particular test performed.

The mainstream flow visualizations were performed on four planes as seen in Fig. 1. These four planes correspond to locations at the upstream edge, the midspan, the downstream edge, and midway between two rows of dimples. Each plane of seeding particles was illuminated with the dual cavity planar laser and visualized with the two high speed Phantom cameras. The entire channel was mounted on a linear traverse to enable accurate and repeatable positioning when moving between planes.

The S-PIV was performed on both V-shaped configurations. For each geometry, the four Reynolds numbers were measured at four discrete planes. The laser plane furthest upstream is located 9.15 hydraulic diameters downstream of the entrance to the dimpled section,

ensuring the fluid boundary layer is fully developed. All S-PIV measurements were completed in an unheated channel. In total, four laser planes for each flow condition and dimple array were examined. The laser planes were 9.15, 9.28, 9.40, and 9.58 hydraulic diameters downstream of the entrance to the heated portion of the channel. These laser planes are centered above the 12 thermocouples that are monitored for the heat transfer portion of this study. Because of the relatively narrow channel, positioning the cameras on the same side of the laser plane would have severely restricted the size of the visible portion of the plane. As a result, the cameras were placed directly above the channel, each with a view of either side of the plane at an oblique angle as seen in Fig. 1.

#### **DATA REDUCTION**

To fully assess the performance of both the in-line and staggered V-shaped dimple arrays, channel averaged heat transfer coefficients are complimented with measurement of the pressure losses through each channel. The heat transfer enhancement is combined with the pressure drop through the channel to compare the overall thermal performance of each channel. Finally, flow field measurements identifying secondary flow patterns and turbulence production due to the dimples are obtained.

#### Channel Heat Transfer Enhancement

For the purposes of this dimpled channel study, a simple steady state heat transfer method was employed to determine the heat transfer coefficient. The steady state method is the most fundamental and simple test that can be employed to determine a heat transfer coefficient. To perform the steady state method, the test surface is heated, while the temperatures of the surface and fluid, as well as the power being consumed by the heater are monitored.

Because not all the heat provided by the heater makes its way to the fluid within the channel, heat losses must be considered. Taking into account heat losses from the channel, the convective heat transfer coefficient can be calculated using Equation 2.

$$h = \frac{Q_{in} - Q_{loss}}{A_s(T_w - T_b)} \tag{2}$$

With the entire heat transfer surface fabricated from a single piece of aluminum, only a single, area averaged heat transfer coefficient is obtained for the plate. This decision was made to simplify the heat transfer portion of the experiment because this overall average heat transfer coefficient is well suited for the purposes of determining how the flow affects heat transfer from the surface and for comparing to regionally averaged data from other studies.

To determine the wall temperature for use in Eqn. 2, the average of the 12 thermocouples directly around the region of interest was taken as the wall temperature for data reduction. This proved to be the most accurate method, matching the Dittus-Boelter correlation for a smooth channel quite well. Due to the high conductivity of the aluminum test surface, this method is regarded as a fair way to average out the expected locally high and low temperatures found in and around the dimples. The bulk fluid temperature was linearly interpolated, from the entrance and exit thermocouples, at a location centered over the 12 thermocouples used for the wall temperature. The surface area was taken as the projected smooth surface area, meaning for all cases, the same surface area, that of a smooth wall, was used.

Determining  $Q_{net}$  accurately is a more complex process. Measuring the total power supplied to the heater,  $Q_{in}$ , however is very straightforward. With the experiment at steady state, the voltage being supplied to the heater is measured along with the resistance of the heater. Determining the amount of energy lost through the external insulation,  $Q_{loss}$ , requires performing a heat loss calibration. To perform

a heat loss calibration, the channel was filled with fiberglass insulation, in an attempt to force as much energy to leave the channel through the external insulation. With the conductivity of the fiberglass insulation less than the surrounding insulation, the majority of heat supplied by the heater conducts though the insulation surrounding the outer surface of the test section. In addition, thermocouples were placed near the test section to measure the ambient room temperature in its vicinity. The temperature difference driving the amount of heat lost from the test section is the difference between the measured wall temperature and the ambient room temperature. This temperature difference accounts for the heat that is first conducted through the surrounding insulation and then transferred away from the test section by either natural convection or radiation. Two heat loss cases were performed, a high and a low heat loss case, at steady state temperatures that bracketed all temperatures seen during any actual heat transfer case. With insulation both inside the channel and surrounding the channel, each data set for the estimation of the heat losses was run for at least five hours until the temperature difference between the wall of the channel and the ambient room approaches a constant value. Linear interpolation was then performed between these two points, for each thermocouple, to account for the heat loss that would be expected from each area of the test plate. Using the first law energy balance, the accuracy of the heat loss approximation was verified. As mentioned previously, the heat transfer coefficients were calculated based on linear interpolation between the measured inlet and outlet bulk temperatures. To validate the heat loss approximation, the heat transfer coefficients were also calculated with the bulk air temperature calculated from the energy balance. With these two methods providing heat transfer coefficients within 6% of one another, the method for approximating the heat loss from the channel is sufficient.

By applying Eqn. 2, the heat transfer coefficient can be determined. While this heat transfer coefficient is important, it is still highly dependent on the characteristics of the channel and the properties of the fluid within the channel. Determining the Nusselt number, Nu, allows the results of this study to be more readily compared to that of previous studies. The Nusselt number is defined as:

$$Nu = \frac{hD_h}{k} \tag{3}$$

To make the enhancements in heat transfer over a smooth channel more apparent, the Nusselt number results can further be normalized by the Dittus-Boelter correlation. When the data is normalized in this manner, is known as the heat transfer enhancement or Nusselt number ratio. The heat transfer enhancement is defined as:

$$HTE = \frac{Nu}{Nu_0} = \frac{Nu}{0.023Re^{0.8} Pr^{0.4}}$$
 (4)

If the heat transfer enhancement continues to increase with respect to Reynolds number, it can be determined that the surface features continue to positively enhance heat transfer, irrespective of the increase in heat transfer associated with simply increasing the Reynolds number.

The experimental uncertainty for the presented results was calculated using the method developed and published by Kline and McClintock [22]. At the Reynolds number of 10000, the overall uncertainty in the Nusselt number ratio is approximately 16% of the presented values. At this lowest Reynolds number, a greater percentage of the heat input is lost. Due to the estimation of these heat losses, the experimental uncertainty increases. However, at the higher Reynolds numbers, the percent uncertainty of the individual measurements decreases and the percentage of heat losses decreases. Therefore, the overall uncertainty in the Nusselt number ratio decreases to approximately 8% of the calculated value at the highest Reynolds number of 37000.

#### Pressure Penalty within the Channel

While the Nusselt number is a very important quantity, it alone is not necessarily the deciding factor to an engine designer. Engine designers are very concerned with the overall flow rate through the channel and trying to ensure the blade is being provided an adequate amount of coolant. If the amount of pressure losses that occur within a channel can be reduced, lower pressure coolant can be used, reducing the use of high pressure coolant to instances where it is absolutely required. This pressure drop is measured in the lab with a micromanometer in inches of water. To be truly useful to an engine designer, the pressure drop must be non-dimensionalized to produce a friction factor. This friction factor allows the designer to determine what the pressure losses would be for their specific channel geometry. With the pressure drop measured, the Darcy friction factor, f, can be determined with the following equation:

$$f = \frac{\Delta P}{\frac{1}{2}\rho V^2} \frac{D_h}{\Delta x} \tag{5}$$

According to the method described by Kline and McClintock [22], the experimental uncertainty in the friction factor ratio is less than 15% for the Reynolds number of 37000. However, at the lower Reynolds numbers, the inlet pressure to the channel decreases, and the experimental uncertainty in the friction factor ratio can exceed 30%.

#### Overall Thermal Performance

Typically an increase in heat transfer comes with an increase in friction factor, increasing pressure losses. If these pressure losses can be avoided, while increasing heat transfer, it would make the use of such a design more attractive to an engine designer. The thermal performance,  $\eta,$  attempts to normalize the heat transfer enhancement data, taking into account the pressure losses associated with a design. The equation for thermal performance is defined as:

$$\eta = \frac{Nu/Nu_0}{\left(\frac{f}{f_0}\right)^{\frac{1}{3}}} \tag{6}$$

The friction factor for turbulent flow within a smooth tube is determined with Equation 7 (Blasius equation):

$$f_0 = \frac{0.316}{\text{Re}^{1/4}} \tag{7}$$

Combining the experimental uncertainties from the heat transfer tests with those to measure the pressure drop within the channel, it is possible to estimate the experimental uncertainty of the overall thermal performance. Over the range of Reynolds numbers considered, the average experimental uncertainty is estimated to 13.5% of the measured value.

#### Stereoscopic Particle Image Velocimetry (S-PIV)

Before collecting data, a spatial calibration was performed with a custom two plane calibration plate. This calibration gives DaVis the required information to accurately calculate velocities in all three dimensions and to account for the viewing angles of each camera. With this spatial calibration complete, a set of data could be collected. At this point, a self-calibration was performed using the DaVis software, further improving the accuracy of the spatial calibration and ensuring the data collected was valid. The remaining data sets for that particular plane could then be recorded and saved.

With the raw image pairs collected, processing of the data could now be completed using the DaVis software. Within the DaVis software, a multi-pass stereo-cross correlation was performed with a decreasing interrogation region size. A total of five passes of cross correlation were performed to produce the velocity fields. Three initial passes were performed at interrogation window sizes of 32 x 32 pixels and a final two passes were performed at 16 x 16 pixels. For each pass, a 50% overlap was used, meaning each interrogation region overlapped the previous region by 50%. A very relaxed post processing filter was performed, removing any vectors that had a signal to noise ratio less than 1.1.

After each image pair was processed, producing velocity vectors for each image pair, the mean velocities and velocity magnitudes could then be calculated at the center of each interrogation regions with the following equations:

$$\overline{u} = \frac{1}{N_i} \sum_{i=1}^{N_i} u_i \tag{8}$$

$$\overline{v} = \frac{1}{N_i} \sum_{i=1}^{N_i} v_i \tag{9}$$

$$\overline{w} = \frac{1}{N_i} \sum_{i=1}^{N_i} w_i$$
 (10)

$$V = \sqrt{\overline{u}^2 + \overline{v}^2 + \overline{w}^2} \tag{11}$$

Due to the accuracies of the high speed controller, cameras, laser, and spatial calibration used with the DaVis software, any uncertainties due to the equipment and measuring systems are expected to be minor in comparison to the random uncertainties introduced by turbulent fluctuations within the channel. These random uncertainties caused by the turbulent fluctuations can be approximated with the equation:

$$U = \frac{t_s S_V}{\sqrt{N_v}} \tag{12}$$

In this study, the maximum RMS fluctuating velocity was observed on the downstream edge of the V-shaped dimples for the highest flow rate, and could reach as high as 4 m/s. As this is the worst case scenario, random uncertainties within the time averaged results would be expected to be less than 0.25 m/s. Considering the large flow rates tested, these uncertainties are well within reason.

#### **RESULTS AND DISCUSSION**

Jordan and Wright [19] used separate transient liquid crystal and transient temperature sensitive paint techniques to show heat transfer enhancement afforded by an in-line array of V-shaped dimples. Both experimental techniques indicated as the Reynolds number of the coolant increases, the heat transfer enhancement also increases (up to their maximum Reynolds number of 40000). The current investigation aims to study the flow behavior above the V-shaped surface to provide insight into the surface heat transfer behavior. Therefore, the results begin with a brief discussion of the overall heat transfer coefficients measured for both the in-line and staggered and dimple arrays. This discussion is followed by flowfield measurements obtained using S-PIV at discrete planes within the dimple array.

### Heat Transfer Enhancement and Thermal Performance

The surface averaged Nusselt numbers are plotted in **Figure 3** as a function of the channel Reynolds number. In addition to the averaged Nusselt numbers measured in the dimpled channels, those measured in a smooth channel are also shown, all with respect to the Nusselt number predicted from the Dittus-Boelter correlation for turbulent flow in a smooth tube. Using the average of the twelve surface thermocouples located in the downstream section of plate proves to be acceptable for obtaining the Nusselt numbers in the fully developed region. As shown in Fig. 3, the Nusselt numbers measured in the smooth channel are within 10% of those predicted by the correlation. When comparing the

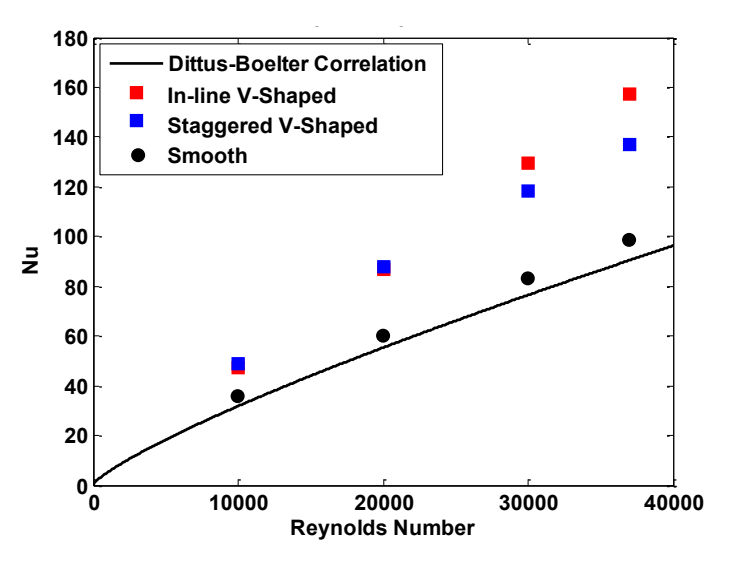


Figure 3: Average Nusselt Numbers for Smooth and Dimpled Channels

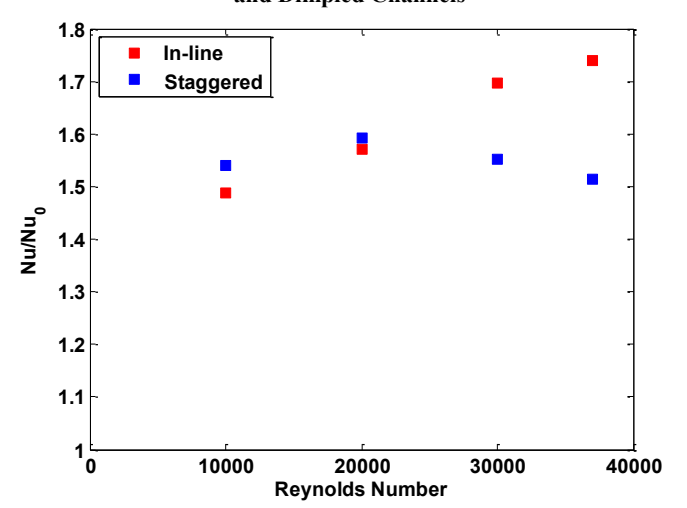


Figure 4: Heat Transfer Enhancement in Dimpled Channels

heat transfer afforded by the two dimple arrays, at the two lower Reynolds number cases, 10000 and 20000, the staggered array very slightly outperformed the in-line array. At the higher Reynolds numbers, 30000 and 37000, the in-line dimple significantly outperformed the staggered array.

Figure 4 reports the heat transfer enhancement results of the two V-Shaped dimpled plates. From Fig. 4, it becomes clear that at Reynolds numbers greater than 20000, the heat transfer enhancement begins to decrease for the staggered array. On the other hand, the in-line array shows an increase with respect to Reynolds number. One could argue that the staggered array is relatively insensitive to changes in Reynolds number (which is consistent with traditional hemispherical dimples). However, it is clear that the in-line array departs from this typical Reynolds number insensitivity. While the magnitude of heat transfer enhancement does not vary significantly between the in-line and staggered arrays (within the experimental uncertainty of the experiment), distinct trends can be observed. As shown by Jordan and Wright [19], the heat transfer enhancement increases with increasing Reynolds number for the in-line array. This increase in heat transfer enhancement with respect to Reynolds number is advantageous over rib turbulated

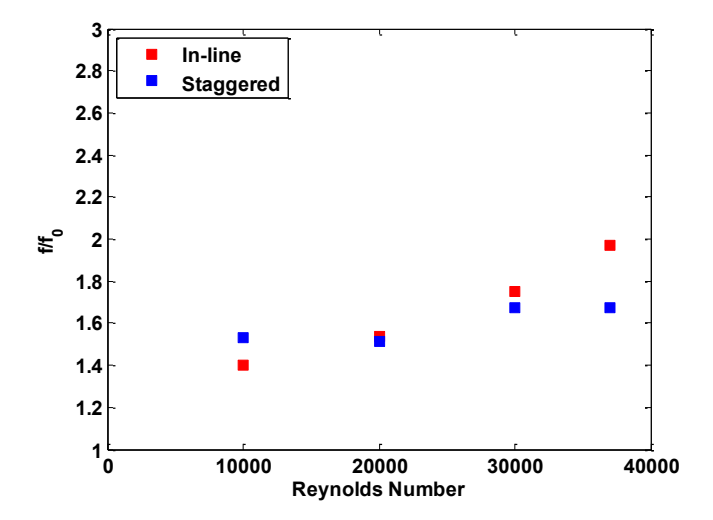


Figure 5: Friction Factor Ratios in the Dimpled Channels

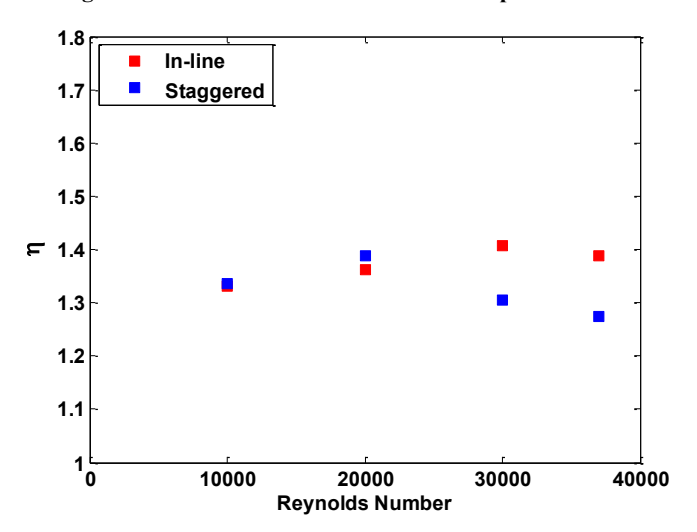
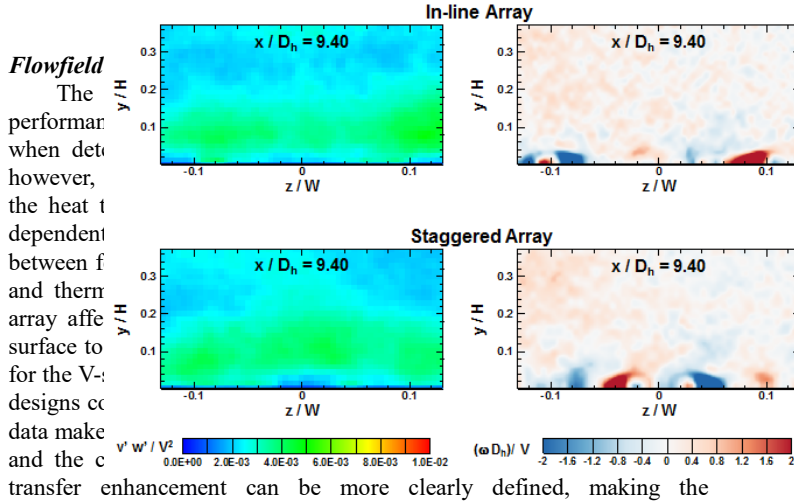


Figure 6: Thermal Performance of Dimpled Channels

passages which exhibit a decrease in heat transfer enhancement as Reynolds numbers increase.

To explore the cost of the heat transfer enhancement, Figure 5 presents the friction factor ratios for both dimpled channels. For the inline array, the friction factor ratio continues to increase as the Reynolds number increases. The staggered array does not show the same clear trend, showing only a very slight increase in friction factor ratio as the Reynolds number increases. From Figs. 4 and 5, it can be concluded that the flow conditions caused by the differences between the two dimpled arrays are significant enough to have a noticeable effect on the heat transfer enhancement and friction factor ratios of the two designs.

With the heat transfer and frictional losses recorded, the thermal performance of each dimple array can be calculated. The thermal performances for both dimpled arrays is presented in Figure 6. As shown in Fig. 4, the heat transfer enhancement of the in-line array very noticeably increases with increases in Reynolds number; however, due to the large pressure penalties incurred at the higher flow rates, the thermal performance actually peaks at 30000. Despite incurring increasingly large pressure penalties at higher Reynolds numbers, the inline array appears more attractive to an engine designer from a heat transfer enhancement and thermal performance perspective.



optimization of the guring in Turbulanth Yelecityd Fluctuations and Vorticity

Time averaged S-PIV restates Dill 2.40 switter for 10000 the in-line and staggered arrays, with differences between the two highlighted. Velocity magnitudes for both arrays at a Reynolds number of 10000 are presented in Figure 7. In this figure (and subsequent figures of the velocity distribution), the velocity vectors have been normalized by the average velocity in the core of the channel. This makes it easy to discern whether particular flow features of the coolant continue to grow stronger, or weaker, with an increase in Reynolds number. The velocity magnitude shown in the contour plots has been normalized by the average velocityinie Alreay-direction. For eastaggered Array (and vorticity) distributions, a small region near the surface has been used. 

+x1 Din= 9115 .

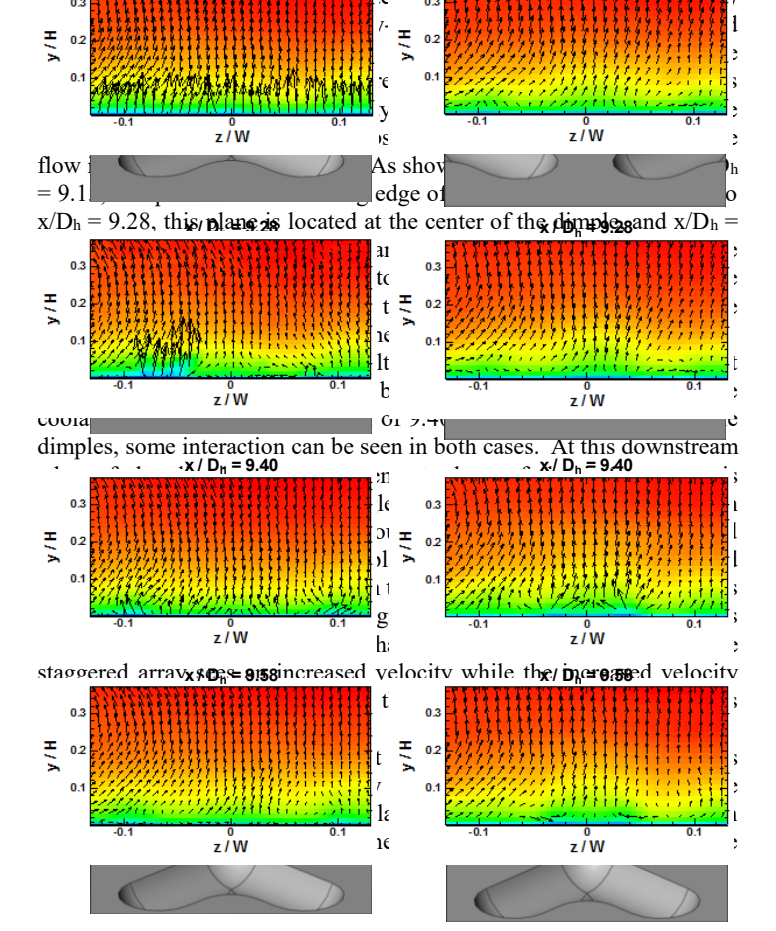


Figure 7: Velocity Distributions with Re = 10000

0.4 0.5

0.2

secondary flows with significantly lower magnitudes than the primary, x component. At the edge of the dimple (x/Dh = 9.40), the staggered array induces a relatively wide band of turbulence that covers nearly 20% of the channel height (0 < y/H < 0.2). This means the staggered array shows a greater capacity to move warmer air from near the surface, through the already thinner buffer layer, and allow it to mix with the cooler core of the flow. This increased mixing with the core of the flow leads to an increase in the rate of heat transfer associated with the staggered array. The vorticity distributions shown in Fig. 8 also indicate distinct counter-rotating vortices emerging from the legs of the two adjacent dimples. In addition to the main vortex pair, it appears contained with the primary vortex, a small second vortex rotating opposite of the primary vortex. The additional mixing leads to increased heat transfer on the plateau region downstream of the dimples of the staggered array.

The velocity distributions at each of the four planes with Re = 20000 are shown in **Figure 9**. When compared to a Reynolds number of 10000, each plane shows a significantly stronger surface to coolant interaction. The buffer layer no longer appears to evenly span the width of the channel, instead distinct pockets of slower moving coolant can be seen near the surface. At this increased flow rate, the flowfield over each surface appears distinct. The flow over the in-line array shows two slower regions of coolant located close to the surface, between dimples (z / W =  $\pm 0.13$ ). The staggered array, on the other hand, shows three slower regions near the surface.

Looking at the staggered array, it is clear the two slower pockets of coolant that appear at z / W locations of -0.13 and 0.13 are a result of each row that has three dimples. These two slower moving pockets match those seen over the inline array. The third slower region of coolant, occurring in the middle of the channel, at a z / W location of 0.0, is a result of each row that has two dimples. Although these pockets contain overall slower moving coolant, they have relatively strong velocities in the y and z directions. This increased movement in the y direction, along with the local increases in turbulence in y and z directions serves to further enhance the heat transfer from the surface. At the furthest upstream plane,  $x / D_h = 9.15$ , where the measurement plane is at the leading edge of each dimple, the pockets of coolant ejected from the previous row can be easily seen. This is a result of the strong ejections of coolant emerging from the downstream edge of the preceding rows of dimples. The upwash regions from the previous rows, in both cases, continue to entrain coolant near the surface, lifting it up into the core of the flow. It is interesting to note that the two pockets of slower moving coolant seen in the in-line case are overall larger than those seen in the staggered case, with stronger velocities in the y direction, but overall weaker velocities in the z direction.

Moving one measurement plane downstream to x /  $D_h$  = 9.28, which is over the midline of the V-shaped dimples, coolant can be seen moving downward into the dimples. For the in-line array, the region from z / W = -0.04 to 0.04, and at y / H < 0.04 appears to slowly enter the dimple. Interestingly, for the case of the staggered array, the y and z direction velocities are observed to be larger in the near wall region, around z / W =  $\pm 0.1$ , being more quickly pulled into the dimples. With a larger amount of coolant entering the dimples in a staggered array, a larger amount of coolant will also impinge within the dimple, taking advantage of the increased heat transfer area afforded by the use of dimples. This difference in the amount of coolant entering the dimples, between the in-line and staggered cases, is related to the location of the upwash regions from the previous row of dimples. For the in-line case,

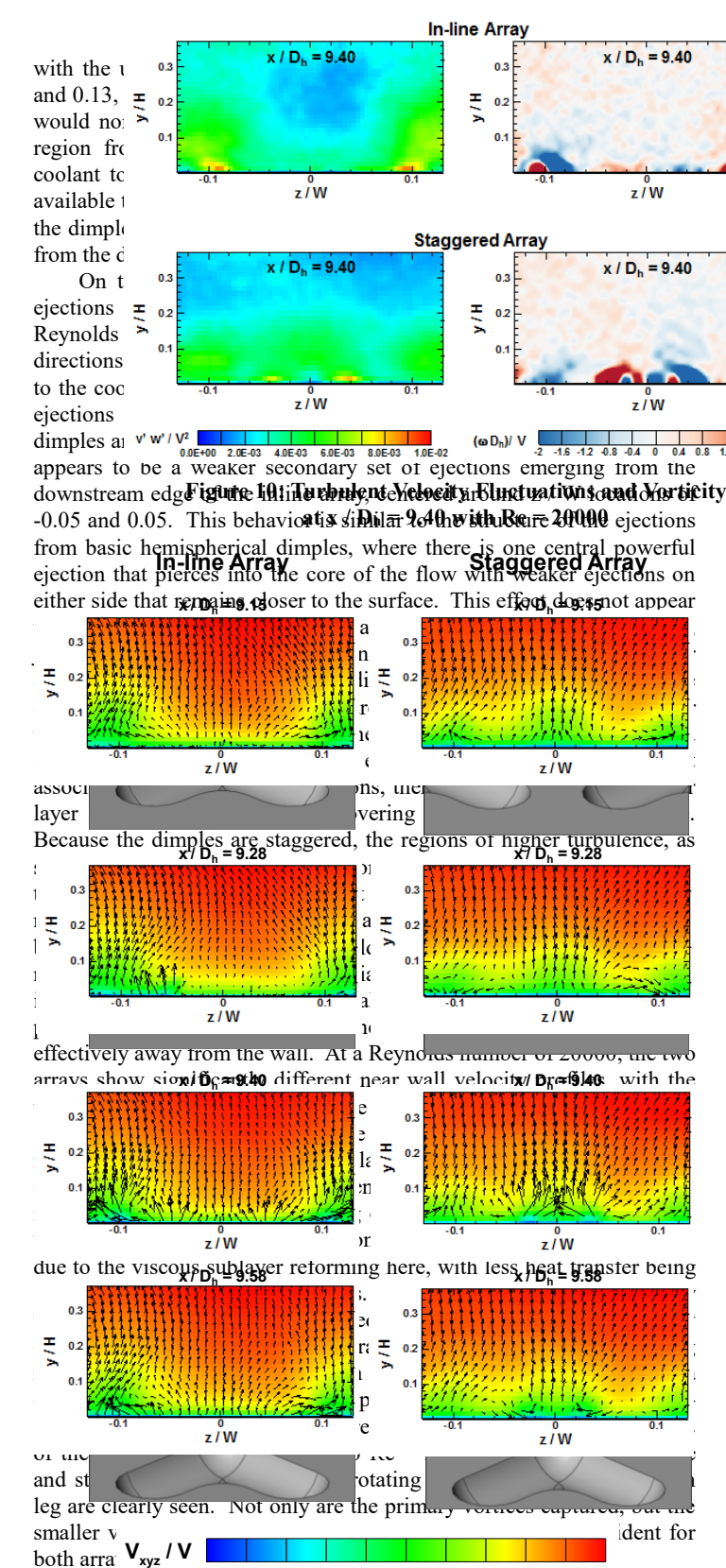


Figure 9: Velocity Distributions with Re = 20000

Further downstream, at x /  $D_h = 9.58$ , the upwash from the previous plane can be seen persisting, although the velocities in the y direction have weakened by approximately 45% for the in-line array and 35% for the staggered array. Like in the preceding plane, stronger y velocities are seen in the case of the staggered array. The stronger upwash increases the amount of entrainment seen, producing higher near wall z velocities as the upwash pulls coolant away from the surface. As a result of the higher y and z velocities, the vortices produced in the staggered case are likewise stronger than seen in the in-line case. stronger vortices seen in the staggered case, coolant is actually seen moving downwards, impinging on the surface before moving toward the upwash region. This, and the overall stronger transverse velocities in the near wall region, lead to a larger portion of coolant being entrained in to the upwash region for the staggered case. For both the in-line and the staggered array, this plane appears similar to  $x / D_h = 9.15$ . This is logical in the case of the in-line array, where every row is identical, one would expect the plane between a row of dimples to be slightly stronger than the plane at the tip of the next row. However, in the case of the staggered array, this observation is perplexing as each row is offset, and therefore, one would expect the plane at x /  $D_h$  = 9.15 to show significant differences to the plane at x /  $D_h = 9.58$ . The similarity of the flow structures on these two planes indicates the flow has become fully developed at these downstream locations.

For an in-line array, these ejections are always around z / W locations of -0.13 and 0.13, due to the dimples always being in line with the dimples from the previous row. Because of this, the ejections from an in-line array tends to exhibit constructive interference, building upon themselves as the flow moves down the channel row by row, leading to very strong upwash regions that entrain a large amount of coolant near the surface and pierce further into the core of the flow, increasing mixing with the cooler core of the flow. In the staggered case, every other row creates an ejection that is half a period offset in the z direction, causing destructive interference, reducing the strength of the ejections from the previous row.

Increasing the channel flow rate to a Reynolds number of 30000 causes some interesting and unexpected changes in the flowfield. The S-PIV results for this case can be seen in **Figure 11**. For only a 50% increase in bulk channel velocity over Re=20000, the PIV data for the in-line array shows around an 85% increase in transverse velocities near the surface. For the staggered array, the increase in near wall velocities more closely follows the increase in bulk velocity, showing an increase in transverse velocities near the surface of just under 50% as compared to the 20000 Reynolds number cases.

Despite the significant differences in the flow in the area close to the wall at Re = 30000, the basic behavior of the flow remains largely the same as the flow in the 20000 Reynolds number cases. On the upstream edge of the dimples, at x /  $D_h$  = 9.15, the in-line case shows the persistent upwash from the ejections of the previous row have strengthened significantly, reaching approximately 30% further into the core of the flow. The staggered case on the other hand shows little visible change (compared to Re = 20000), with the upwash regions from the previous row not piercing noticeably further into the core of the flow. On closer inspection, while the velocities in the y direction did in fact increase in magnitude, they actually decreased relative to the 50% increase in channel velocity, as visualized by the normalized velocity vectors becoming shorter. The in-line case on the other hand shows the y velocities in the upwash region increasing by a significant amount, showing absolute increases of approximately 125%.

Moving one plane downstream, at the mid-plane of the dimples,  $x / D_h = 9.28$ , similar differences are seen. The in-line case again shows persistent upwash regions, from the previous row's ejections, piercing

further into the core of the flow. The upwash regions again do not appear to change over the staggered array. Both the in-line and the staggered array do show an increase in the amount of coolant that is entering the dimples. Recall for Re = 20000, the region of

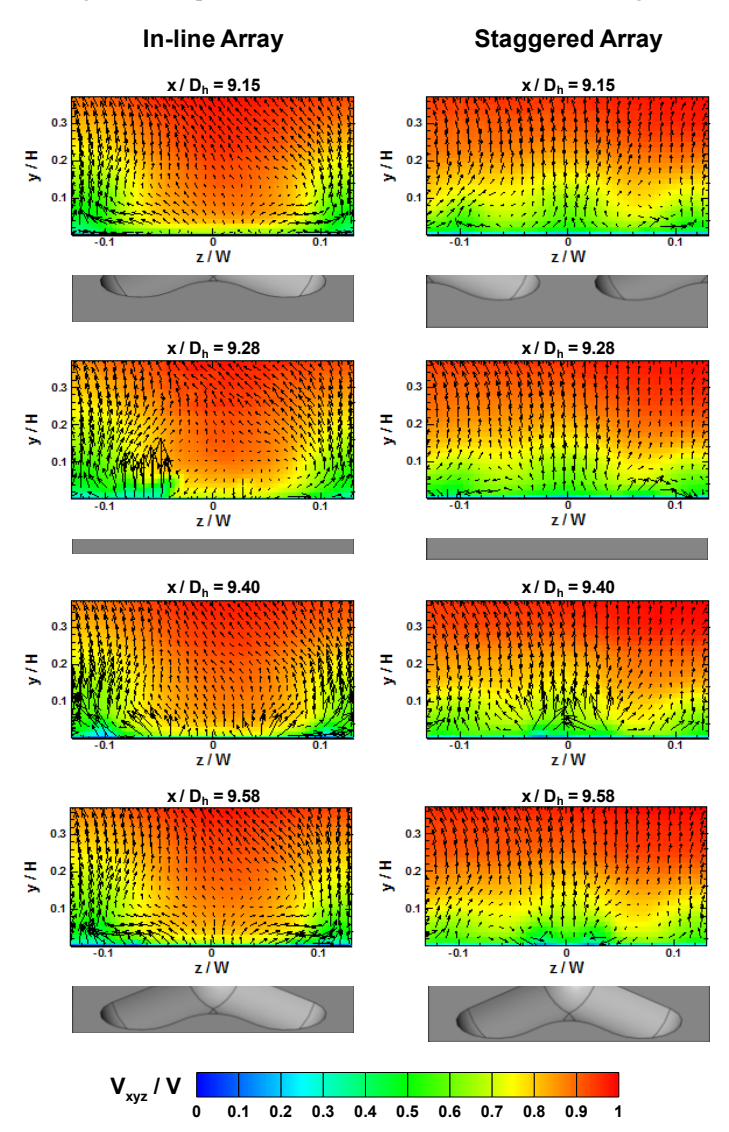


Figure 11: Velocity Distributions with Re = 30000

-0.4 < z / W < 0.04, and y / H < 0.04, contained very short vectors pointing into dimple cavity. For Re = 30000, the region with velocity vectors in the negative y direction has grown to a height of y / H = 0.1, with the velocities also increasing significantly in the negative y direction. The staggered case also shows more coolant entering the V-shaped dimple, with the normalized velocity vectors growing in the areas surrounding the dimples; however, this increase in coolant entering the dimple is minor compared to the increase in the amount of coolant entering the dimple for the in-line array.

Data from the downstream edge of the dimples, for both the in-line and staggered cases, show few changes in the basic structure of the flow between a Reynolds number of 20000 and 30000. The most notable change to the structure of the flow is again seen in the in-line case, where the upwash region reaches higher into the core of the flow. With only a 50% increase in bulk channel velocity over the 20000 Reynolds

number case, the vertical component of velocity seen in the upwash region on the downstream edge of the inline dimples more than doubles. The staggered array shows little more than a 50% increase in the vertical component of velocity, again tracking close to the increases seen in the bulk velocity. Both of these conclusions are again supported by the observations of the amount of coolant that appears to be entering the dimple on the previous plane. As observed with Re = 20000, the in-line array again exhibits the secondary ejections occurring centered around  $z/W = \pm 0.05$ . This phenomena is again absent in the in the flowfield over the staggered array. It is interesting to note that this secondary flow structure does appear to exit the dimple with considerable force, with velocities approximately 80% of that of the more prominent ejections from the branches of the dimples. Their effect on the overall flow structure remains relatively weak, with only slight differences seen in adjacent vectors, suggesting that this effect is likely very quickly lost to the highly turbulent nature of the flow.

Further downstream, at the midplane between rows of dimples, x/D<sub>h</sub> = 9.58, the upwash regions for both arrays again weaken compared to the preceding plane. However, on this plane the y velocities over the in-line array are seen to weaken by approximately 30%. The staggered array shows an even greater reduction in y velocities compared to the previous plane, with a 40% loss. Recall for Re = 20000, the in-line and staggered arrays showed losses of 45% and 35%, respectively. At a Reynolds number of 30000, the trend has changed, with the staggered case showing greater losses. Despite these differences, the flowfields for both the in-line and staggered cases appear similar to the flowfields seen at the leading edge of the V-shaped dimples for each respective array. This is again perplexing as one would expect the flow field observed at x /  $D_h$  = 9.15 for the staggered array to show the two upwash regions at  $z/W = \pm 0.13$  to be stronger than the upwash region at z / W = 0. This is not the case, with the central upwash region remaining the strongest for all four measured planes.

The increased mixing is confirmed with the turbulence intensity distributions shown in **Figure 12**. At the downstream edge of the dimples (x /  $D_h = 9.40$ ), not only is the dimple induced turbulence increasing, but the mixing covers a larger area within the channel. While both the staggered and in-line arrays produce very defined vortices exiting the dimples, the structure created by the staggered array remains close to the surface. The circulation created by the in-line array begins to break down around y / H = 0.1. The strength of the vortices decreases as they lift off the surface. However, this lift off is enhancing mixing with the core of the coolant.

When looking at S-PIV data alone, comparing two different flow fields, it is not always easy to discern which would produce the greatest heat transfer enhancement, as was the case at Re = 10000 and 20000. The S-PIV data at Re = 30000 is much more clear. The very strong, persistent upwash regions produced by the in-line array pierce far into the core of the flow, all the while, entraining large amounts of coolant near the surface, and mixing it with the core of the flow. The staggered array does create upwash regions; however, they never reach as far into the core flow or entrain as much coolant from the near surface region. Also, the flow is generally slower across the entirety of the surface. All of these traits would suggest the heat transfer for the staggered array would be less than that seen in the inline array. Figure 4 clearly shows at Re = 30000, the in-line array provides more heat transfer enhancement compared to the staggered array.

Looking at the S-PIV results at Re = 37000, as seen in **Figure 13**, it appears the trends observed between Remolds numbers of 20000 and 30000 continue. Once again, for less than a 33% increase in the mainstream velocity, transverse velocities near the surface over the inline array increased, on average, 78% over Re = 30000. For the

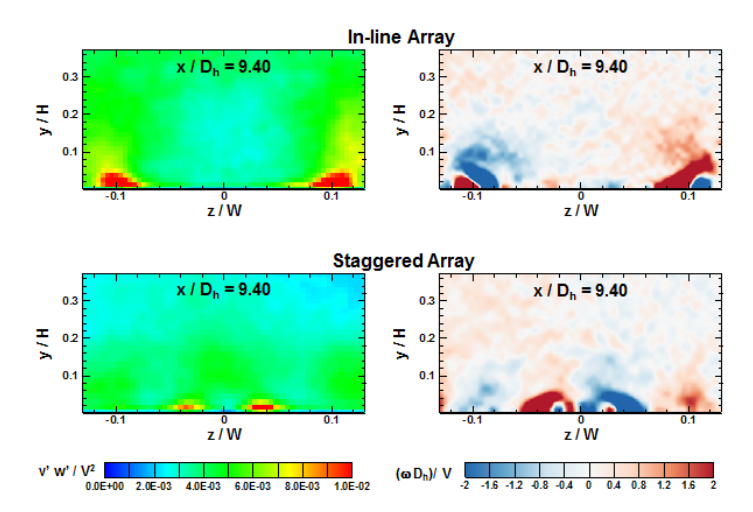


Figure 12: Turbulent Velocity Fluctuations and Vorticity at  $x / D_h = 9.40$  with Re = 30000

staggered array, the near wall, transverse velocities only increased 22% over those at Re = 30000. This suggests there is less activity in the near wall region for the staggered array at Re = 37000 than at Re = 30000.

At the leading edge of the V-shaped dimples, x /  $D_h$  = 9.15, close inspection of the normalized S-PIV data of the in-line array shows that the in-plane velocities of the upwash regions actually decrease in strength, by about 5% versus the 30000 Reynolds number case. Along with the decrease in in-plane velocities for the inline array, the staggered array once again performs significantly worse, showing a normalized loss of in-plane velocities in the central upwash region of 30% versus the 30000 Reynolds number case. The in-line case also shows the formation of a region where the in-plane velocities appear stagnant, spanning from -0.05 < z / W < 0.05 at a height y / H = 0.12. The staggered array does not show this effect.

At the mid-plane section of the rows of V-shaped dimples,  $x\,/\,D_h=9.28,$  the in-line array again shows a decrease in in-plane velocities amounting to 5% when normalized by the mainstream velocity, versus the same plane at a Reynolds number of 30000. More interestingly the region that includes the portion of the flow that is moving into the dimple cavity has again grown in height significantly. The region now spans from -0.04 < z / W < 0.04 and up to a height of y / H = 0.18, up from y / H = 0.1 at Re = 30000. From 30000 to 37000, the normalized velocities in this area have more than doubled, suggesting an even larger amount of coolant is entering the dimple. The staggered array shows weakening in-plane velocities across the board, with the upwash region weakening by a normalized 27%. The small pockets that appear to enter the dimple cavity likewise appear to have shrunk further, exhibiting weaker velocities in this location as well.

At the downstream edge of the dimples, at  $x/D_h=9.40$ , the strength of the ejections for both arrays changes considerably. The normalized velocities for the ejections from the in-line array increase 20% over that of the 30,000 Reynolds number case. This again agrees with the earlier observation of larger amount of coolant entering the dimples. It is also interesting considering the previous planes have shown reductions in the normalized velocities seen in the upwash regions. The secondary ejection is again present and strengthening as well, showing a 13% increase in normalized velocities. This could potentially lead to a slower reattachment of the viscous sublayer. The staggered array shows at 26% decrease in normalized velocities within the upwash regions (compared to Re = 30000). This suggests the ejections from the staggered region are not capable of piercing as far into the mainstream flow.

At the mid-plane between rows of dimples,  $x/D_h = 9.58$ , it is clear that the effects of the very large ejections dissipate quickly. Compared to the previous plane, the velocities in the upwash region have decreased 48%. This rapid degradation of the vortices is likely due to the intense turbulence centered over the two ejections from the in-line array.

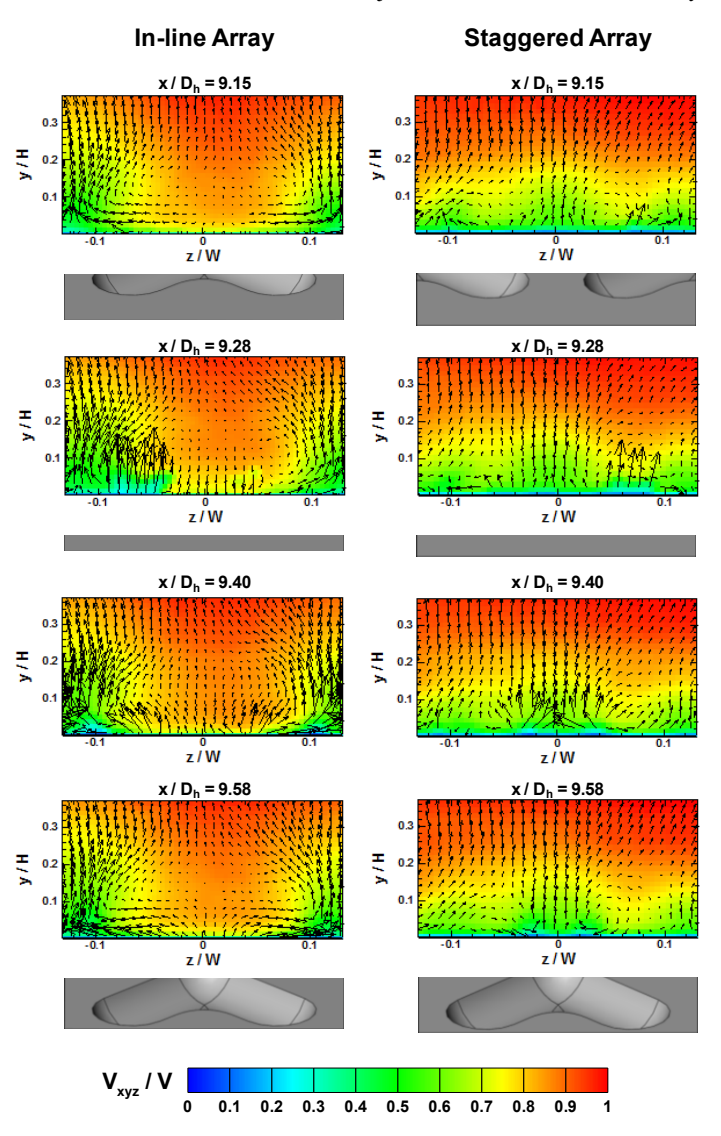


Figure 13: Velocity Distributions with Re = 37000

Despite this rapid loss in energy, the upwash regions do exhibit a 12% increase in normalized velocities compared to the 30000 Reynolds number cases. This is especially interesting considering the flowfield at the leading edge of the next row of dimples is likely to mirror that of the leading edge of the current row, including a 5% decrease in normalized velocities, continuing the rapid degradation of the flow structure. The stagnation region noted at the leading edge of the dimples is seen forming at this plane, with exceptionally strong transverse velocities below it, preventing coolant from disrupting this region. The flow over the staggered array again appears less organized than at lower Reynolds numbers, exhibiting a decrease in normalized upwash velocities of 10%.

**Figure 14** shows similar turbulence and vorticity distributions as those for Re = 37000. The vortical structure induced by the staggered dimples is well-defined but remains close to the surface. Above the in-

line array, the dimple induced vortices have grown to occupy a significant area of the channel. Furthermore, for the staggered array, the relative turbulence intensity at the exit of the dimple has actually decreased compared to Re = 30000. With the secondary flows above the in-line array strengthening with increasing Reynolds number, it is clear

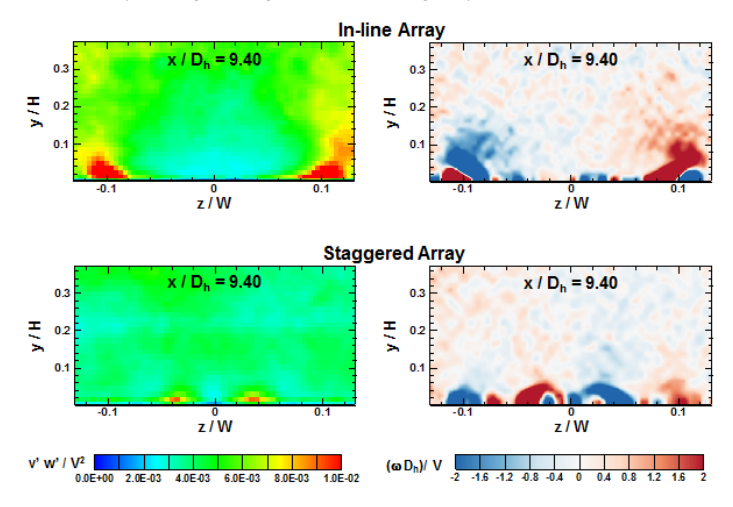


Figure 14: Turbulent Velocity Fluctuations and Vorticity at x /  $D_h$  = 9.40 with Re = 37000

why the heat transfer enhancement also increases.

The effect of Reynolds number on the vorticity measured at  $x / D_h = 9.58$  is shown in **Figure 15**. This figure shows how the vortices change as the Reynolds number increases. On this plane located midway between two dimple rows, there is minimal variation in the flow structure of the vortices induced by the staggered array. This is consistent with results from traditional hemispherical dimple studies where the heat transfer enhancement is relatively insensitive to Reynolds number. However, with the in-line array, at the lowest Reynolds number of 10000, the flow appears disorganized. As the Reynolds number increases, the vortices emerging from the upstream dimple become apparent. With the Reynolds number increasing to 30000 and 37000, these vortices are energized and begin lifting off the surface. These counter-rotating vortices are enhancing the mixing of the warm air near the surface with the core of the coolant near the center of the channel. This mixing pulls the cooler fluid to the wall, and thus the heat transfer from the dimpled wall increases.

#### **CONCLUSIONS**

The secondary flows induced by V-shaped dimples have been investigated in this experimental study. Prior work by Jordan and Wright [19] showed an array of in-line V-shaped dimples offered continued heat transfer enhancement with increasing Reynolds number. This observation was particularly interesting as the heat transfer enhancement provided by traditional hemispherical dimples is relatively insensitive to the Reynolds number, and the Nusselt number ratios in ribbed channels decrease with increasing Reynolds number. The current investigation used a steady state heat transfer trend to confirm that the Nusselt number ratios in a channel with an array of in-line V-shaped dimples increase with increasing Reynolds number. These results were compared to a staggered array of V-shaped dimples for which the Nusselt number ratios decreased with increasing Reynolds number.

Using stereo-particle image velocimetry (S-PIV), it was shown the secondary flows induced within the in-line array have a constructive interaction from row-to-row within the channel. As the vortices migrate

downstream through the channel, they interact with the vortices created in the subsequent downstream rows. The counter-rotating vortices continue to gain strength and induce mixing within the channel. As the vortices lift of the channel wall, the core of the mainstream coolant is pulled toward the wall to efficiently remove heat from the channel wall. As the Reynolds number increases within the channel, the vortices are energized, and their structure begins to break down as they lift off the dimpled surface. The increased turbulence further enhances heat transfer within the channel.

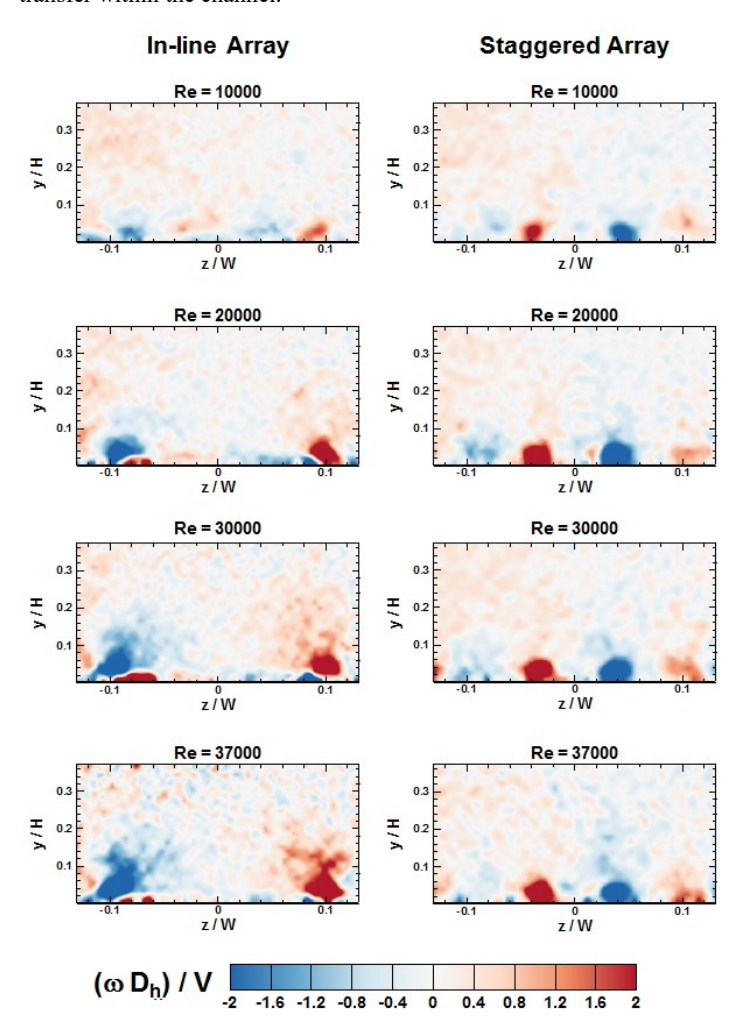


Figure 15: Reynolds Number Effect on Vorticity at  $x / D_h = 9.58$ 

The staggered array of V-shaped dimples also induce counterrotating vortices. However, as the vortices of two subsequent rows interact, the vortices are weakened as the vortices are rotating in opposite directions. Due to this destructive interaction, the vortices are unable to lift off the surface, and they are suppressed near the channel wall. With limited mixing with the core coolant flow, heat transfer from the dimpled wall is reduced compared to the in-line array.

With knowledge of the secondary flow patterns created by the Vshaped dimple arrays, it is possible to further increase heat transfer within these channels by optimizing the dimple array. Both the geometry of the dimple (diameter, depth, and angle of the V) and the array (spanwise and streamwise spacing) can begin to be optimized. Furthermore, the V-shaped dimple should be investigated at Reynolds numbers beyond 40000 to investigate if the Nusselt number ratios continue to rise at elevated Reynolds numbers. With the advancement of computational resources and turbulence models, CFD could provide an efficient means to optimize the V-shaped dimple geometry while providing a more in depth understanding of the underlying flow physics.

#### **ACKNOWLEDGEMENTS**

This work has been sponsored by the National Science Foundation under award number CBET-1126371. The authors would like to thank Dr. Truell Hyde, Vice-Provost of Research at Baylor University, and Dr. William Jordan, Mechanical Engineering Department Chair, for their support of this project.

#### **REFERENCES**

- [1] Han, J.C., Dutta, S., Ekkad, S., 2013, Gas Turbine Heat Transfer and Cooling Technology, Taylor & Francis, Florida, 869 pages.
- Gromov, P.R., Zobin, A.B., Rabinovich, M.I., and Sushchik, M.M., 1986, "Creation of Solitary Vorticies in a Flow Around Shallow Spherical Depressions" Sov. Tech. Phys. Lett., Vol. 12, pp. 1323-
- Lin, Y. L., Shih, T. I-P., and Chyu, M. K., 1999, "Computations of Flow and Heat Transfer in a Channel with Rows of Hemispherical Cavities," ASME Paper No. 99-GT-263.
- Mahmood, G. I., Hill, M. L., Nelson, D. L., Ligrani, P. M., Moon, H.K., Glezer, B., 2001, "Local Heat Transfer and Flow Structure on and Above a Dimpled Surface in a Channel" ASME J.
- Turbomachinery, Vol. 123, pp. 115-123.
  Mahmood, G. I. and Ligrani, P. M., 2002, "Heat Transfer in a Dimpled Channel: Combined Influences of Aspect Ratio, Temperature Ratio, Reynolds Number, and Flow Structure" *Int. J.*
- Heat Mass Transfer, Vol. 45, pp. 2011–2020. Ligrani, P.M., Harrison, J.L., Mahmood, G.I., and Hill, M.L., 2001, "Flow Structure due to Dimple Depressions on a Channel Surface" Physics of Fluids, v 13 No. 11, pp. 3442-3451.
- Won, S. Y., Zhang, Q., and Ligrani, P. M., 2005, "Comparisons of Flow Structure Above Dimpled Surfaces with Different Dimple
- Depths" *Physics of Fluids*, v 17, pp. 045105-1-9. Chyu, M.K., Yu, Y., Ding, H., Downs, J.P., and Soechting, F.O., 1997, "Concavity Enhanced Heat Transfer in an Internal Cooling Passage" ASME Paper No. 97-GT-437. Moon, H.K., O'Connell, T., and Glezer, B., 2000, "Channel Height
- Effect on Heat Transfer and Friction in a Dimpled Passage" ASME
- J. Engineering for Gas Turbines and Power, Vol. 122, pp. 307-313.

  [10] Kim, Y.W., Arellano, L., Vardakas, M., Moon, H.K., and Smith, K.O., 2003, "Comparison of Trip-Strip/Impingement/Dimple Cooling Concepts at High Reynolds Numbers" ASME Paper No. GT2003-38935
- [11] Burgess, N.K., Oliveira, M.M., and Ligrani, P.M., 2003, "Nusselt Number Behavior on Deep Dimpled Surfaces Within a Channel" *ASME J. Heat Transfer*, Vol. 125, pp. 11-18.

  [12] Bunker, R.S. and Donnellan, K.F., 2003, "Heat Transfer and Frintion Factors for Flows Inside Circular Tubes with Concavity
- Surfaces" ASME Paper No. GT2003-38053.
- [13] Moon, S.W. and Lau, S.C., 2002, "Turbulent Heat Transfer Measurements on a Wall with Concave and Cylindrical Dimples in a Square Channel" ASME Paper No. GT-2002-30208.
- [14] Chyu, M.K., Yu, Y., and Ding, H., 1999, "Heat Transfer Enhancement in Rectangular Channels with Concavities" *J. Enhanced Heat Transfer*, Vol. 6 pp. 429-439.
- [15] Isaev, S.A., Leont'ev, A.I., and Baranov, P.A., 2007, "Simulating Tornado-Like Enhancement of Heat Transfer under Low-Velocity Motion of Air in a Rectangular Dimpled Channel. Part 2: Results of Parametric Studies" *Thermal Engineering*, Vol. 54, No. 8, pp. 655-
- [16] Borisov, I., Khalatov, A., Kobzar, S., and Glezer, B., 2004, "Comparison of Thermo-Hydraulic Characteristics for Two Types of Dimpled Surfaces" ASMÉ Paper No. GT2004-54204.
- [17] Khalatov, A. and Onishchenko, V., 2008, "Heat Transfer and Surface Frection Downstream of a Dual Array of Dimples of a Different Shape" ASME Paper No. GT2008-50022
- Zhou, F. and Acharya, S., 2009, "Experimental and Computational Study of Heat/Mass Transfer and Flow Structure for Four Dimple Shapes in a Square Internal Passage" ASME Paper No. GT2009-60240.

[19] Jordan, C.N. and Wright, L.M., 2013, "Heat Transfer Enhancement in a Rectangular (AR = 3:1) Channel with V-Shaped Dimples," ASME J. Turbomachinery, Vol. 135, No. 1, Article 011028 (10

pages).

[20] Liou, T.M., Chang, S.W., Chen, J.S., and Chan, C.Y., 2009, "Fluid Flow Inside a Rectangular Duct with Two Opposite Walls Roughened by Deepened Scales," ASME Paper No. GT2009-59302.

[21] Griffith, T.S., Al-Hadhrami, L., and Han, J.C., 2003, "Heat Transfer in rotating Rectangular Cooling Channels (AR = 4) With Dimples" *ASME J. Turbomachinery*, Vol. 125, pp. 555-564.
[22] Kline, S.J., and McClintock, F.A., 1953, "Describing Uncertainties in Single-Sample Experiments," Mech. Eng. (Am. Soc. Mech. Eng.), 75, pp. 3-8.